

Role of critical thickness in SiGe/Si/SiGe heterostructure design for qubits F

Cite as: J. Appl. Phys. **132**, 085302 (2022); <https://doi.org/10.1063/5.0101753>

Submitted: 10 June 2022 • Accepted: 02 August 2022 • Published Online: 30 August 2022

 Yujia Liu, Kevin-P. Gradwohl,  Chen-Hsun Lu, et al.

COLLECTIONS

 This paper was selected as Featured



View Online



Export Citation



CrossMark

ARTICLES YOU MAY BE INTERESTED IN

Multiferroic antiferromagnetic artificial synapse

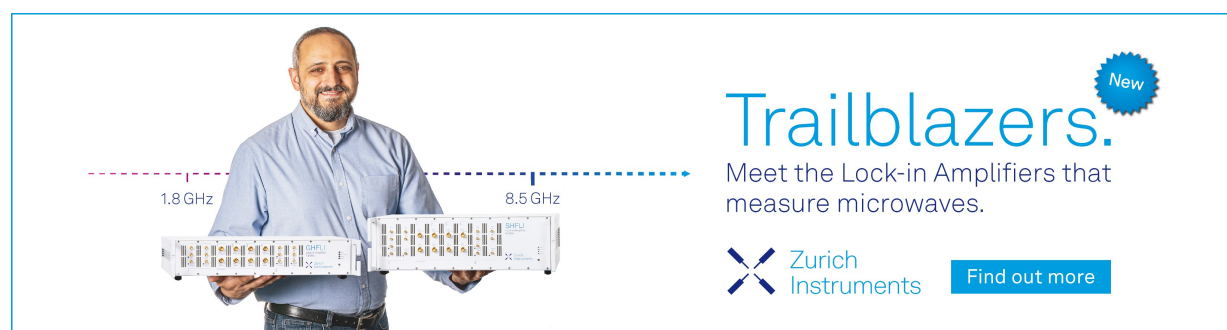
Journal of Applied Physics **132**, 084102 (2022); <https://doi.org/10.1063/5.0084468>

A brief review of reconstructions and electronic structures of MoS₂ zigzag edges

Journal of Applied Physics **132**, 080702 (2022); <https://doi.org/10.1063/5.0098639>

Microscopic probing of the doping effects of In ions in Fe₃O₄

Journal of Applied Physics **132**, 083904 (2022); <https://doi.org/10.1063/5.0091339>



Trailblazers. New

Meet the Lock-in Amplifiers that measure microwaves.

 Zurich Instruments [Find out more](#)

Role of critical thickness in SiGe/Si/SiGe heterostructure design for qubits

Cite as: J. Appl. Phys. **132**, 085302 (2022); doi: [10.1063/5.0101753](https://doi.org/10.1063/5.0101753)

Submitted: 10 June 2022 · Accepted: 2 August 2022 ·

Published Online: 30 August 2022



Yujia Liu,^{1,a)}  Kevin-P. Gradwohl,¹  Chen-Hsun Lu,¹  Thilo Remmele,¹ Yuji Yamamoto,²  Marvin H. Zoellner,²  Thomas Schroeder,^{1,3} Torsten Boeck,¹ Houari Amari,¹ Carsten Richter,¹  and Martin Albrecht¹ 

AFFILIATIONS

¹Leibniz-Institut für Kristallzüchtung, Max-Born-Straße 2, 12489 Berlin, Germany

²IHP—Leibniz-Institut für Innovative Mikroelektronik, Im Technologiepark 25, D-15236 Frankfurt(Oder), Germany

³Institut für Physik, Humboldt-Universität zu Berlin, Newtonstr. 15, 12489 Berlin, Germany

^{a)}Author to whom correspondence should be addressed: yujia.liu@ikz-berlin.de

ABSTRACT

We study the critical thickness for the plastic relaxation of the Si quantum well layer embedded in a SiGe/Si/SiGe heterostructure for qubits by plan-view transmission electron microscopy and electron channeling contrast imaging. Misfit dislocation segments form due to the glide of pre-existing threading dislocations at the interface of the Si quantum well layer beyond a critical thickness given by the Matthews–Blakeslee criterion. Misfit dislocations are mostly 60° dislocations ($b=a/2 \langle 110 \rangle$) that are split into Shockley partials ($b=a/6 \langle 112 \rangle$) due to the tensile strain field of the Si quantum well layer. By reducing the quantum well thickness below critical thickness, misfit dislocations can be suppressed. A simple model is applied to simulate the misfit dislocation formation and the blocking process. We discuss consequences of our findings for the layer stack design of SiGe/Si/SiGe heterostructures for usage in quantum computing hardware.

© 2022 Author(s). All article content, except where otherwise noted, is licensed under a Creative Commons Attribution (CC BY) license (<http://creativecommons.org/licenses/by/4.0/>). <https://doi.org/10.1063/5.0101753>

I. INTRODUCTION

Electron spins confined in top-gated Si quantum wells are excellent candidates for realizing reliable solid state based qubits.^{1,2} Such qubits have noticeable advantages over other qubit technologies: (i) their industrial production is compatible with today's advanced Si manufacturing technology, which benefits the scalability of the quantum computing hardware and (ii) they can be produced such that they are free of nuclear spin by utilizing isotope-enriched ^{28}Si , which leads to unrivaled spin coherence times.³ Compared to Si electron qubits at a Si/SiO₂ interface, established strain engineering concepts developed for SiGe heterostructures permit tuning the valley splitting.^{4,5}

There are several factors that should be taken into consideration for designing Si_{1-x}Ge_x/Si/Si_{1-x}Ge_x stacks for gate-based quantum computing hardware. Sufficient tensile strain in the quantum well layer has to be provided to lift the sixfold valley degeneracy and create a sufficiently large energy splitting. However, the Si quantum well layer needs to have a sufficient thickness to

ensure quantum confinement. Furthermore, strain fluctuations due to interface steps, alloy fluctuations, and dislocations have to be minimized in order to avoid uncontrollable potential fluctuations, which in turn alter the effective valley splitting.^{6,7}

Strained Si quantum well layers are realized on relaxed Si_{1-x}Ge_x buffers with a Ge content x of $0.25 < x < 0.33$. These buffers are grown on Si substrates, where the mismatch strain is relaxed by misfit dislocation networks in the lower interfaces. However, the misfit dislocations are often terminated by threading segments propagating to the surface, typically leading to threading dislocation densities between 1×10^5 and $1 \times 10^7 \text{ cm}^{-2}$. In this paper, we study the impact of such threading dislocations on the strain relaxation of the Si quantum well layers and discuss the critical thickness in terms of the model presented by Matthews and Blakeslee.⁸ While the relaxation of strained Si quantum well layers on relaxed SiGe buffers has first been studied by Ismail *et al.*, the authors focused on the impact of misfit dislocations and their strain field on electrical transport.⁹

Examining the requirements of SiGe/Si/SiGe stacks for quantum circuits, increasing the strain of the Si quantum well layer can be realized by growing on relaxed SiGe buffers with a higher Ge content. However, when both strain and film thickness are high, the Si thin film may start to relax as the strain energy exceeds a critical value for the generation of defects such as misfit dislocations. This results in strain inhomogeneities in the quantum well layer that affect the band structures and may perturb the electron wave function as well as the device performance.

In this work, we present a detailed experimental study on the misfit dislocation formation in tensile strained Si quantum well layers and present a simple model that accounts for dislocation pinning in these thin layers and quantitatively reproduces the observed dislocation network. Our work is based on the contrast analysis of the dislocation distribution by transmission electron microscopy (TEM) and electron channeling contrast imaging (ECCI). We study identical heterostructures grown on buffers with different threading dislocation densities as well as samples with quantum well layers of different thicknesses on identical buffers. We show that misfit dislocations form above the critical thickness defined by the Matthews–Blakeslee criterion.

II. GENERAL CONCEPTS

The classical concept of misfit dislocation formation by threading dislocation gliding has been presented by Matthews and Blakeslee.⁸ Here, a pre-existing threading dislocation is extended at the interface between a strained layer and the substrate once the Peach–Köhler force acting on the threading segment in the layer exceeds its line tension. Since the force on the threading segment scales linearly with its length, this happens beyond a critical thickness as displayed in the inset of Fig. 1.

The critical thickness can be calculated by the balance between the force exerted on threading dislocation by misfit strain F_E and the line tension of the misfit dislocation generated at the interface F_L . To calculate the critical thickness h_c for a Si quantum well layer on a $\text{Si}_{0.7}\text{Ge}_{0.3}$ relaxed buffer, we apply the adaption of the criterion presented by People and Bean based on the Matthews–Blakeslee theory,¹⁰

$$h_c \approx \frac{b}{4\pi f(1+\nu)} \left(\ln \frac{h_c}{b} + 1 \right), \quad (1)$$

where $b = 0.384 \text{ nm}$ is the Burgers vector, $\nu = 0.28$ is the Poisson ratio, and f is the lattice mismatch between Si and the relaxed SiGe virtual substrate. This equation is adjusted for epitaxial layers on thick substrates, which corresponds to our case of the Si thin film on thick SiGe virtual substrates.

The critical thickness of Si depends on the mismatch strain and hence on the Ge content in the buffer. This dependency is plotted for a fully relaxed SiGe buffer in Fig. 1. The strained Si on $\text{Si}_{0.7}\text{Ge}_{0.3}$ has a critical thickness of 8.5 nm, where $\text{Si}_{0.7}\text{Ge}_{0.3}$ is the commonly used relaxed buffer layer for Si electron qubits.^{5,11}

One should mention that strained $\text{Si}_{1-x}\text{Ge}_x$ layers on dislocation free Si substrates can be grown coherently and fully strained far beyond this thickness. This is due to the absence of threading dislocations, which means that dislocations that can relax the strain have to nucleate first. This nucleation of dislocations is a thermally activated

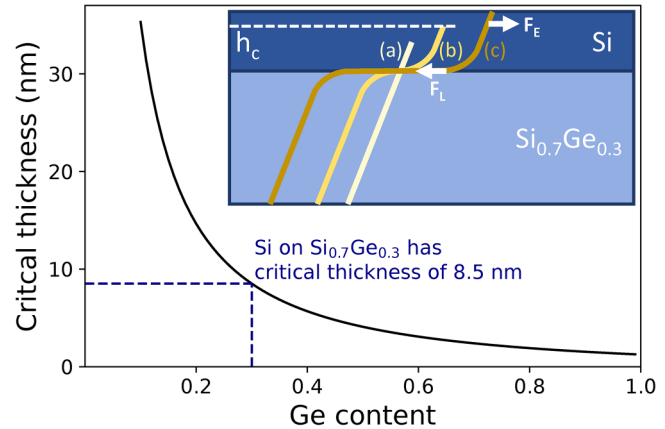


FIG. 1. Critical thickness of an epitaxial Si layer as a function of Ge content x in relaxed $\text{Si}_{1-x}\text{Ge}_x$ buffer. The inset illustrates the elongation of a grown-in threading dislocation forming a misfit dislocation: (a) if no misfit is present, the threading dislocation tends to be straight; (b) when the misfit strain is present, the threading dislocation tends to bend; and (c) once the epitaxial layer exceeds a certain critical thickness, the force from the misfit strain exerted on the threading dislocation F_E is larger than the force resulting from the extension of the dislocation F_L . Hence, the threading dislocation glides leaving behind a misfit dislocation segment at the interface.

process with higher energy barrier than threading dislocation gliding and depends on the thermal budget of the growth process.^{10,12}

In the following, we will show that, in our case, where sufficient threading dislocations are present, the Matthews–Blakeslee criterion is met and the relaxation of the quantum well layer depends on the threading dislocation density in the buffer. We also show that threading dislocations are pinned when intersecting other perpendicular misfit dislocations in this case, because the thickness of the quantum well layer is not thick enough for dislocations to overcome the barrier, exposed by the misfit dislocation at the interface, which results in a particular arrangement of the misfit dislocations.

III. EXPERIMENTAL DETAILS

Epitaxial growth of the four SiGe/Si/SiGe heterostructures investigated in this work was carried out by utilizing a reduced pressure chemical vapor deposition (RPCVD) system. Standard p-type Si (001) wafers are used. After HF cleaning, the wafer is loaded into the RPCVD reactor and baked at 1000°C in H_2 to remove residual oxide. Then, the wafer is cooled down to the SiGe growth temperature. Step gradient SiGe layers were deposited using a $\text{SiH}_4\text{--GeH}_4$ gas mixture with H_2 carrier gas. Finally, a thick 30% constant composition SiGe layer is deposited. In order to enhance relaxation and improve the crystal quality of the relaxed SiGe buffer, annealing in H_2 is performed after each SiGe deposition step. After the final annealing, the strained Si layer is deposited using a $\text{H}_2\text{--SiH}_4$ gas mixture at 700°C . For two samples (referred to as “A” and “B”), an upper SiGe cap is deposited using the same process condition followed by an additional 3 nm Si cap for surface protection. The schematic layer stacks of the samples are listed in Fig. 2.

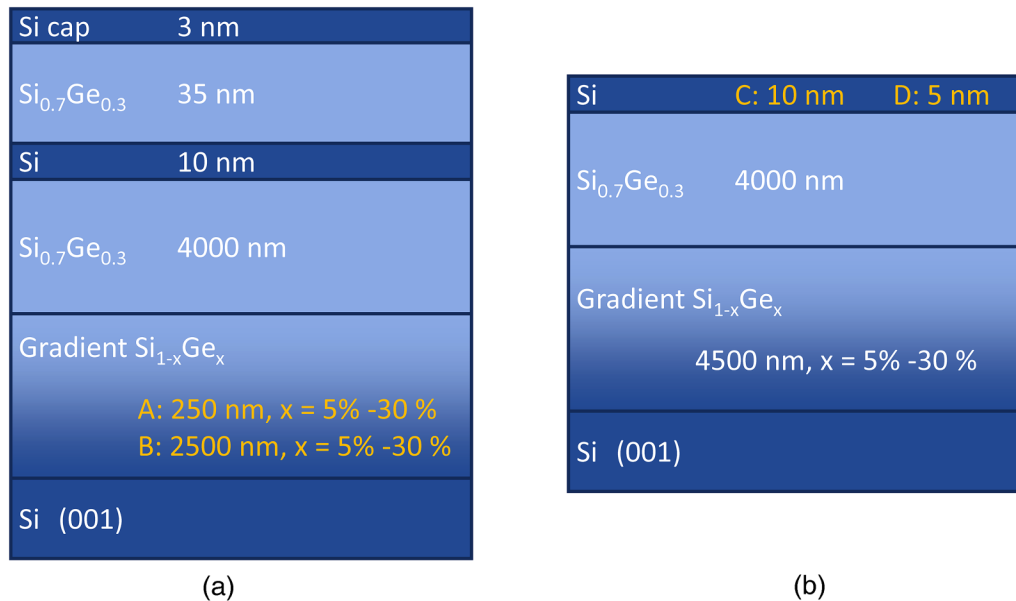


FIG. 2. Schematic structure of the investigated SiGe/Si/SiGe heterostructure: (a) samples A and B with the different bottom SiGe buffer layers, indicated by the yellow text and (b) samples C and D with the different Si top layer thickness, indicated by the yellow text.

The TEM investigations of dislocations in the samples were carried out using an aberration corrected FEI Titan 80-300 TEM, operated at 300 kV. The plan-view TEM samples were mechanically polished from the substrate side down to $10\ \mu\text{m}$ in the thickness by a series of diamond abrasive films with decreasing grain sizes. Then, argon ion beam milling was performed from the same site on the samples with a Gatan's Precision Ion Polishing System (PIPS) under an incident angle of the ion beams of 5° and an accelerating voltage of 3 kV. Polishing from the backside maintains the original growth surface and allows us to follow the defects from the SiGe buffer into the Si quantum well layer. The acceleration voltage was reduced to 0.2 kV, in order to remove the amorphous layer from the TEM sample surfaces.

ECCI measurements were performed in a Thermo Fisher Scientific's Apreo scanning electron microscope (SEM), operated at 10 kV, and an approximate beam current of 3.2 nA. The images were taken by the in-lens detector (T1) which is located at the entry of the pole piece and acts as an integrated annular back-scattered electron detector. It allows for backscatter images at voltages as low as 2 kV.

To measure the threading dislocation densities of the relaxed buffer layers, we rely on Secco defect etching, which is analyzed in the SEM.

IV. RESULTS AND DISCUSSION

A. Misfit dislocation observation in the SiGe/Si/SiGe heterostructure

Figure 3 presents typical examples of TEM bright field images taken under different diffraction conditions to analyze

the dislocation distribution in SiGe/Si/SiGe. Here, we focus on the impact of the different threading dislocation densities in the buffers A and B on the relaxation of the Si quantum well layer. According to defect-selective etching, the relaxed buffer of sample A has a threading dislocation density of $1.4 \times 10^7\ \text{cm}^{-2}$ [Figs. 3(a) and 3(b)] and the relaxed buffer of sample B has threading dislocation density of $3 \times 10^5\ \text{cm}^{-2}$ [Figs. 3(c) and 3(d)]. For clarity, we show here exclusively bright field images using 220 and $2\bar{2}0$ reflections since they already express the main features. The dislocations are numbered consecutively. The main features of both samples can be discussed taking as example dislocations 2, 8, and 9. Dislocation 2 has a long threading segment at the right hand side coming from the buffer. It bends into the (001) plane and forms a misfit segment lying along the $[1\bar{1}0]$ direction. It has a short threading segment at the left end. The long misfit segment has a characteristic double contrast in 220 and appears as a single line in $2\bar{2}0$ reflection. From the geometry, i.e., the length of the threading segments, we conclude that the long segment at the right hand side is a threading dislocation that comes from the SiGe buffer and forms the misfit dislocation at the interface of the quantum well layer, while the left hand threading segment is the one that penetrates the surface. The double contrast is due to the splitting of a perfect 60° dislocation, for example,

$$\frac{a}{2}[101] \rightarrow \frac{a}{6}[112] + \frac{a}{6}[2\bar{1}1]. \quad (2)$$

Dislocation 8 has very similar contrast behavior, which means it is split to two partial dislocations, for example,

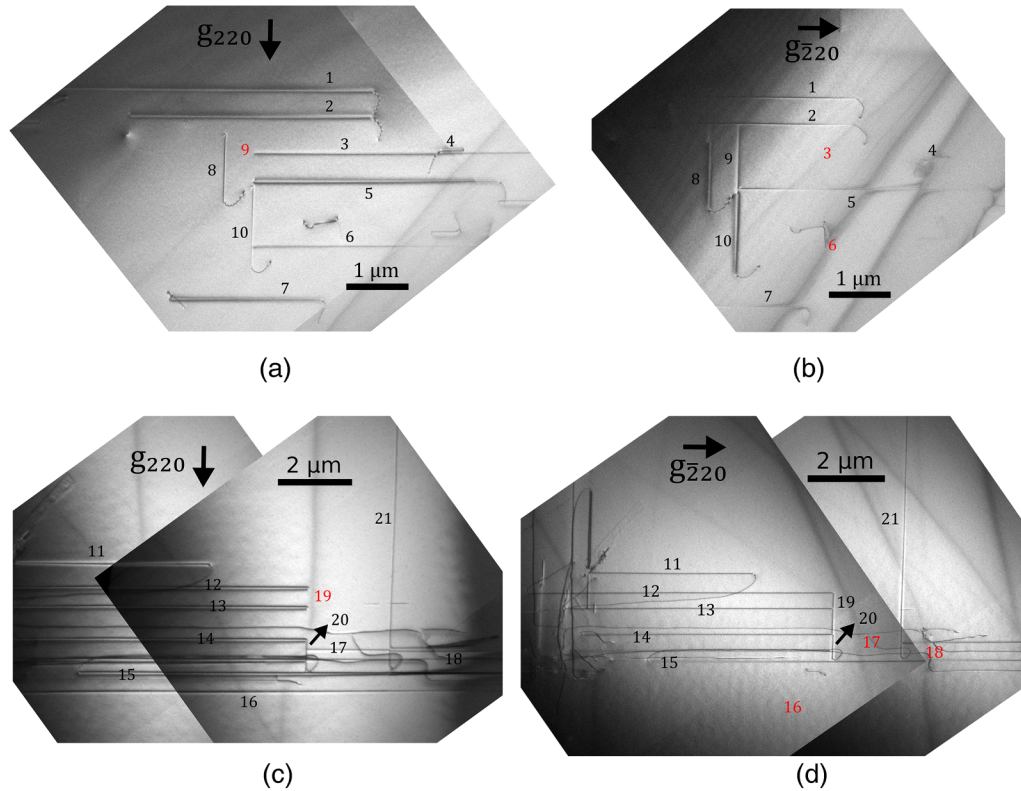


FIG. 3. Plan-view TEM images of SiGe/Si/SiGe heterostructures on different SiGe virtual substrates: (a) and (b) presenting sample A with the virtual substrate having a threading dislocation density of $1 \times 10^7 \text{ cm}^{-2}$ and (c) and (d) presenting sample B with the virtual substrate having a threading dislocation density of $3 \times 10^5 \text{ cm}^{-2}$. The diffraction vectors g are indicated by black arrows. The misfit dislocations are numbered consecutively, whereas the invisible dislocations are numbered in red color. The crystallographic orientations of the misfit dislocations are noted in the [Appendix](#).

$$\frac{a}{2} [101] \rightarrow \frac{a}{6} [1\bar{1}2] + \frac{a}{6} [211]. \quad (3)$$

Respectively, dislocation 9 vanishes at the 220 reflection and is present at the $2\bar{2}0$ reflection, which indicates a 90° dislocation or more specifically a Lomer dislocation.¹³ From the spatial arrangement of dislocation 9, we may infer that it has formed by the interaction between two 60° dislocations 5 and 10.¹⁴ Similarly, the 90° dislocation 19 can be explained by a reaction between 60° dislocations 14 and 20. All dislocations analyzed in samples A and B can be assigned to these basic characteristics for a detailed analysis into [Table II](#) in the [Appendix](#). All 60° misfit dislocations are a result of the bending of pre-existing threading dislocation in the buffer: the misfit dislocations are split into Shockley partials. In the TEM images such as [Fig. 3](#) over areas of 5×7 and $10 \times 15 \mu\text{m}^2$, we find that 70% of the misfit dislocations are 60° dislocations while 30% are 90° dislocations. Noticeably, the dislocations 5, 6, and 3 are blocked at dislocations 9 and 10.

Samples A and B show qualitatively a similar structure but are distinguished quantitatively by the spacing of the misfit dislocations at the interface. [Table I](#) compares the threading

dislocation spacings obtained from defect-selective etching of the buffer to misfit dislocations spacing obtained from the TEM images. Here, the

$$\text{Misfit dislocation spacing} = \frac{A}{\sum l}, \quad (4)$$

where l is the length of each individual misfit dislocation and A is the area of the image. The sum is performed over all misfit dislocations in the images of each sample. The threading dislocation spacing is calculated from the threading dislocation density according to

$$\text{Threading dislocation spacing} = \frac{1}{\sqrt{\text{TDD}}}. \quad (5)$$

where TDD is the threading dislocation density. The threading dislocation spacing is around three times the misfit dislocation spacing in both samples A and B.

TABLE I. TDS vs MDS. Here, TDS and MDS indicate threading dislocation spacing and misfit dislocation spacing.

Sample	TDS (μm)	MDS (μm)	TDS/MDS
A	3.2	1.1	2.91
B	18.3	6.4	2.86
C	6.2	1.8	3.4

B. Thickness effects on dislocations in strained Si on SiGe

The analysis in A has shown that the 10 nm thick quantum well layer is above the critical thickness and that each individual threading dislocation transforms into a misfit dislocation according to the model proposed by Matthews and Blakeslee. In the following, we present results from Si quantum well layers with thicknesses above (10 nm) and below (5 nm) the critical thickness according to the Matthews–Blakeslee criterion grown on identical $\text{Si}_{0.7}\text{Ge}_{0.3}$ buffer layers with a threading dislocation density of $8 \times 10^6 \text{ cm}^{-2}$. For analysis of the relaxation by misfit dislocations, we rely on ECCI, which is sensitive to dislocations located in the sample stack close to the surface and permits to scan large areas compared to TEM.

Figure 4(a) shows a typical ECCI image of sample C using the 400 reflection. Two perpendicular sets of misfit dislocations aligned with $[110]$ and $[1\bar{1}0]$ are visible. Similar to the results obtained by TEM, we find that misfit dislocations are related to threading dislocation segments at one of their ends (examples are indicated with yellow arrows). In almost all cases, the other end is an intersection with another, perpendicular misfit dislocation line (examples are indicated with blue arrows). Figure 4(b) shows a corresponding

ECCI image of sample D under identical imaging conditions. Here, no misfit dislocations can be observed, but a few spots with contrast indicated by yellow arrows can be threading dislocations.

In order to compare our results on samples A and B, the misfit and threading dislocation spacing of sample C from Fig. 4(a) is quantified in Table I. The factor between the threading dislocation spacing and the misfit dislocation spacing in sample C is 2.95, similar to sample A and sample B. This striking similarity in the factor among all samples suggests that there is a distinct relation between threading dislocation spacing and misfit dislocation spacing, independent of the threading dislocation density of the buffer.

C. Relationship between misfit and threading dislocation spacing based on geometric considerations

The results for samples A, B, and C indicate that threading dislocations entail misfit dislocation segments as a consequence of glide. Misfit dislocation segments grow in length until the gliding threading segment is blocked by a perpendicular misfit dislocations, as can be seen in Figs. 3(a)–3(d) and 4(a). It is obvious that, with an increasing threading dislocation density in a heterostructure, the number of misfit dislocations increases and, hence, the probability of misfit dislocations being blocked by other misfit dislocation increases. Consequently, the misfit dislocation length has to decrease with increasing threading dislocation density or decreasing threading dislocation spacing [Eq. (5)]. However, the exact relation between threading dislocation spacing and misfit dislocation spacing is not trivial. Here, we will try to shed light on this relation by comparing our experimental results to simulated misfit dislocation networks generated by a Monte Carlo approach.

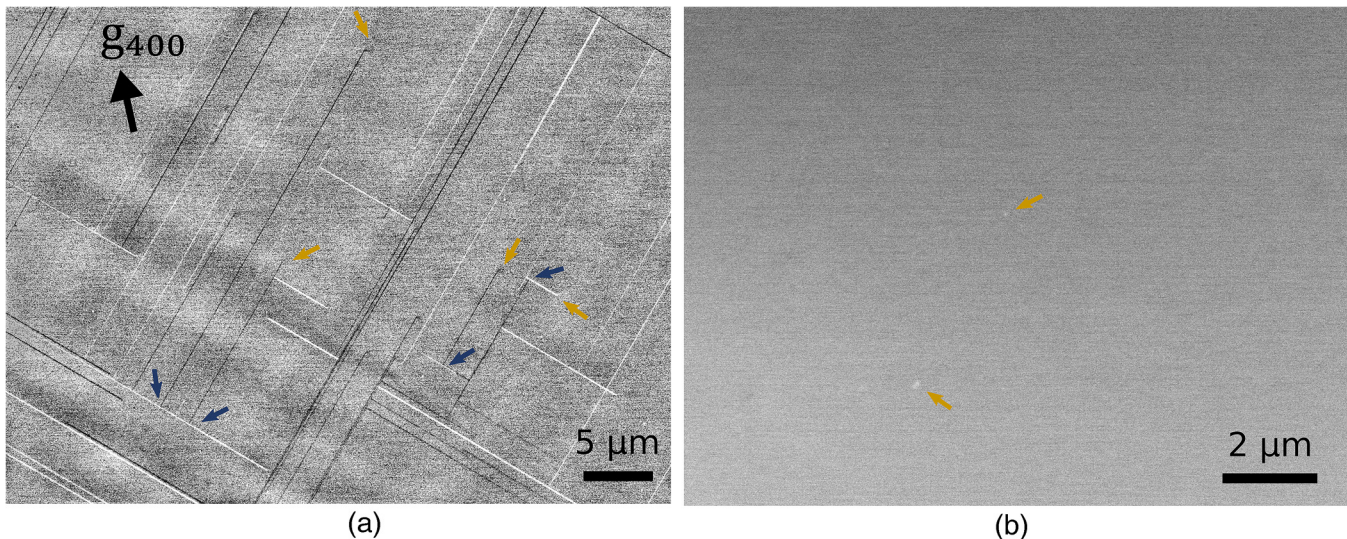


FIG. 4. Electron channeling contrast images showing dislocations in the Si/SiGe heterostructure: (a) sample C—10 nm Si on relaxed SiGe buffer and (b) sample D—5 nm Si on relaxed SiGe buffer. In sample C, misfit dislocations are present as lines with bright or dark contrast along in-plane $\langle 110 \rangle$ directions. Yellow arrows indicate the examples of threading dislocations. Blue arrows indicate the examples when misfit dislocations meet perpendicular misfit dislocations.

For the purpose of this geometric investigation of the misfit dislocation network at the Si/SiGe interface, a simple Monte Carlo simulation has been set up. Fundamentally, this model should evaluate the TDS/MDS ratio based on a misfit dislocation network originating from a random distribution of threading dislocations that glide and leave behind misfit dislocation segments. The glide is assumed to be blocked at intersections with other misfit dislocation segments. The necessary assumptions are depicted in Figs. 5(a)–5(c). First, a random distribution of threading dislocations is chosen, which are represented as intersecting points on a two-dimensional plane parallel to the interface [Fig. 5(a)]. We assume that a misfit dislocation is formed from every threading dislocation on this plane. The line directions of the forming misfit dislocations are constrained to the four $\langle 110 \rangle$ directions at the (001) Si/SiGe interface, as defined by the glide system and as observed experimentally. Hence, every point in the plane (threading dislocation) is assigned to one of four misfit dislocation directions with equal probability, as represented in Fig. 5(b). Afterward, the misfit dislocations elongate until they are blocked by another misfit dislocation or the sample edge, as illustrated in Fig. 5(c). One has to mention that different boundary conditions—such as periodic or non-periodic boundary conditions—have been investigated but did not have a significant impact on the result and are, hence, not further discussed.

An exemplary misfit dislocation structure resulting from these assumptions with a random set of 500 threading dislocations is shown in Fig. 5(d). The resemblance with the misfit dislocation structure obtained by the ECCI measurements in Fig. 4(a) is

striking. It is possible to evaluate the misfit dislocation spacing and threading dislocation spacing according to Eqs. (4) and (5), which yields a ratio between threading dislocation spacing and misfit dislocation spacing of 2.5 for this specific configuration in Fig. 5(d). Figure 5(e) shows the ratio TDS/MDS of 1000 calculated misfit dislocation configurations based on random threading dislocation configurations with an increasing number of threading dislocations ranging from 10 to 10 000. The simulation size is arbitrary and has no impact on the misfit dislocation structure and consequently the ratio between TDS/MDS. The ratio TDS/MDS fluctuates due to the random positions of threading dislocations and misfit dislocation line directions for each simulation. However, the ratio tends toward $\text{TDS/MDS} = 3$ with an increasing number of threading dislocations in the simulation. We address the deviations of this ratio at low numbers of threading dislocations to boundary effects. The ratio of 3 seems to be a purely geometric factor arising from the blocking of misfit dislocations by misfit dislocations in SiGe and is in agreement with the experimentally determined ratios of samples A, B, and C (Table I). Modified assumptions were tested and yielded similar results. More specifically, all models yield a constant ratio between threading dislocation spacing and misfit dislocation spacing for a sufficiently high number of threading dislocations.

Comparing the TDS/MDS values from Table I with the simulation, the dislocation numbers in the view of electron microscopy are limited. Therefore, the experimental values are supposed on the left edge of the simulation in Fig. 5(e), where the TDS/MDS value is close to 2 with a relatively large deviation. The errors from the

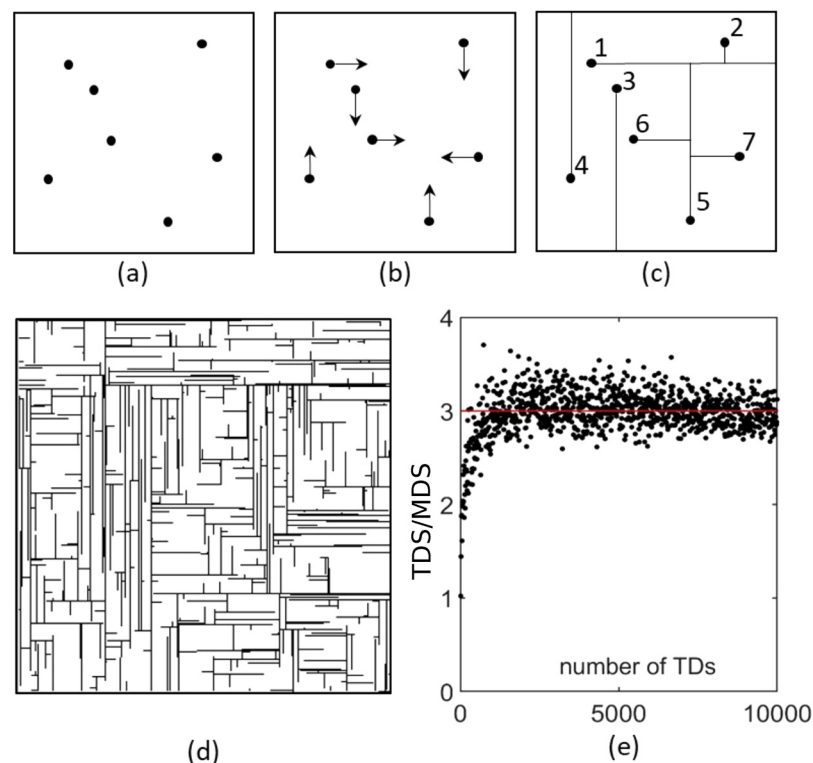


FIG. 5. Schematic showing: (a) random distribution of threading dislocations; (b) random selection of one of the four $\langle 110 \rangle$ misfit dislocations directions at the (001) Si/SiGe interface; (c) misfit dislocations growing one by one until blocked by another misfit dislocations or reaching the sample edge; (d) exemplary misfit dislocation structure arising from the described model; and (e) threading dislocation spacing/misfit dislocation spacing from a set of simulations with varying number initial threading dislocations.

experimental values are likely impaired by the biased electron microscopy investigation.

V. CONCLUSIONS

To conclude the misfit dislocation generation mechanism in SiGe/Si/SiGe heterostructures, we may summarize the main electron microscopy results in Figs. 3 and 4.

- (1) All Si quantum well layers that are thicker than the critical thickness given by the Matthews–Blakeslee criterion (samples A, B, and C) exhibit misfit dislocations at the interface between the quantum well layer and the relaxed buffer.
- (2) All analyzed misfit dislocations in samples A, B, and C have a line direction along $\langle 110 \rangle$. These misfit dislocation segments form due to the glide of threading dislocations pre-existing in the relaxed SiGe buffer as described by Matthews and Blakeslee. The $\langle 110 \rangle$ directions of the glide are defined by the intersection of the $\{111\}$ glide planes and the (001) interface.
- (3) The majority of the misfit dislocations in samples A and B (70%) are 60° dislocations, while the rest are Lomer dislocations.
- (4) Most 60° dislocations are split into Shockley partials. The splitting of 60° dislocation is a typical feature of misfit dislocations accommodating at tensile strain due to the competition between energetic favorite and strain releasing efficiency of partial dislocations.¹⁵ Therefore, it can be concluded that these misfit dislocations are located at the tensile strained layer, which means at the interface between the SiGe buffer layer and the Si quantum well layer.
- (5) Dislocations that meet perpendicular misfit dislocations at the interface are blocked and cannot further extend at the given quantum well layer thicknesses.
- (6) Quantitative evaluation of the threading dislocation spacing and the misfit dislocation spacing shows that their ratio has a factor of approximately 3, independent of the threading dislocation density in the respective buffer. This was simulated by a Monte Carlo method.

From these findings, we conclude that the presence of threading dislocations in the relaxed buffer leads to the formation of misfit dislocation segments at the interface of the Si quantum well layer, as soon as the critical thickness of the quantum well layer as defined by Matthews and Blakeslee is exceeded. We also find that, at the given thickness of the quantum well layer, misfit dislocations block the glide of threading dislocations and, thus, the further extension of misfit dislocations.¹⁶ It is worth mentioning that the blocking mechanism can be overcome when a thicker quantum well layer is grown. When the layer thickness is beyond another critical value, the forces from misfit strain on the threading dislocation segments are greater than the blocking forces from the perpendicular misfit dislocations, which results in the unblocking of the misfit dislocation. According to the theoretical work of Freund,¹⁷ this other critical thickness of the quantum well layer studied in this work is around 20 nm for dislocation unblocking. The quantum well layers in SiGe/Si/SiGe heterostructures for qubit applications are commonly way below this value.

The mechanism of misfit dislocation formation from threading dislocation gliding was often purposely promoted for the strain relaxations in epitaxial layers in order to minimize the generation of new threading dislocations during the strain relaxation, such as epitaxial Ge or SiGe layers on Si (001) substrates.^{12,18,19} However, in the study, a fully strained Si quantum well layer is required, so the occurrence of this mechanism is not desired.

These findings are relevant for the design of SiGe/Si/SiGe heterostructures for spin qubits since dislocations at the interface of the quantum well layer lead to strong local fluctuations of strain and, thus, the valley splitting of the Si conduction band.^{7,20,21} While threading dislocations in these structures might be tolerable to a certain degree because they only make up a small area, misfit running inside the silicon quantum well layer interface affect a large fraction of the film and will likely have negative impact on the qubit device. Although a higher valley splitting of the Si conduction bands is realized through a higher Ge concentration in the SiGe buffer, which leads to larger tensile strain, the critical thickness for plastic relaxation will at the same time be reduced, as shown in Fig. 1. Therefore, a trade-off balancing these two effects needs to be made.

Regarding the kinetics, the activation barrier of the misfit dislocation formation due to pre-existing threading dislocation gliding when exceeding the critical thickness is low. The activation energy may easily be overcome by the CVD growth temperature. A way to prevent relaxation in these structures exhibiting threading dislocations could be to reduce growth at temperatures low enough to prevent dislocation glide. Molecular beam epitaxy gives the possibility, where the growth can be performed at temperatures as low as 350°C . However, the post-growth processing temperatures that are currently used in semiconductor device fabrication highly exceed this temperature and hence pose a limit to this approach.

Methodologically, our work shows that electron channeling contrast imaging is a versatile tool for analyzing the relaxation of epitaxial layers at an early stage and in thin layers, where conventional x-ray diffraction techniques are not sensitive enough.²²

ACKNOWLEDGMENTS

The authors acknowledge Dr. Tobias Schulz for his careful reviewing and discussion. The authors acknowledge the financial support by the Federal Ministry of Education and Research (BMBF) of Germany in the project QUASAR (Project No. 13N15659) and the Leibniz Association in the project SiGe Quant (Project No. K124/2018).

AUTHOR DECLARATIONS

Conflict of Interest

The authors have no conflicts to disclose.

Author Contributions

Yujia Liu: Conceptualization (equal); Data curation (equal); Formal analysis (equal); Methodology (equal); Visualization (equal); Writing – original draft (equal). **Kevin-P. Gradwohl:** Conceptualization (equal); Data curation (equal); Software (equal); Supervision (equal); Validation (equal); Visualization (equal); Writing – original draft (equal); Writing – review & editing

(equal). **Chen-Hsun Lu:** Methodology (equal); Writing – review & editing (equal). **Thilo Remmele:** Methodology (equal). **Yuji Yamamoto:** Methodology (equal); Resources (lead); Writing – original draft (supporting); Writing – review & editing (supporting). **Marvin H. Zoellner:** Conceptualization (equal); Writing – review & editing (lead). **Thomas Schroeder:** Funding acquisition (equal); Investigation (equal); Project administration (equal). **Torsten Boeck:** Funding acquisition (equal); Investigation (equal); Supervision (equal); Writing – review & editing (supporting). **Houari Amari:** Methodology (equal). **Carsten Richter:** Conceptualization (equal); Funding acquisition (equal); Supervision (equal); Writing – review & editing (lead). **Martin Albrecht:** Conceptualization (lead); Formal analysis (equal); Funding acquisition (equal); Methodology (equal); Project administration (equal); Supervision (equal); Visualization (equal); Writing – review & editing (lead).

DATA AVAILABILITY

The data that support the findings of this study are available from the corresponding author upon reasonable request.

APPENDIX: DISLOCATION ANALYSIS

Table II shows the summary of the Burgers vector analysis for misfit dislocations of sample A and B depicted in Fig. 3.

TABLE II. Summary of the Burgers vector analysis for misfit dislocations of sample A and B depicted in Fig. 3. The “✓” indicates visibility of the misfit dislocations in the respective diffraction conditions or that they split into dislocation partials, while the “X” indicates invisibility or that they do not split. The last column of the table presents the dislocation types.

Sample	Dislocation No.	Line direction	Line			Type
			g_{220}	$g_{\bar{2}20}$	Split	
A	1	$[1\bar{1}0]$	✓	✓	✓	60°
	2	$[1\bar{1}0]$	✓	✓	✓	60°
	3	$[1\bar{1}0]$	✓	X	X	90°
	4	$[1\bar{1}0]$	✓	✓	X	60°
	5	$[1\bar{1}0]$	✓	✓	✓	60°
	6	$[1\bar{1}0]$	✓	X	✓	90°
	7	$[1\bar{1}0]$	✓	✓	✓	60°
	8	$[110]$	✓	✓	✓	60°
	9	$[110]$	X	✓	X	90°
	10	$[110]$	✓	✓	✓	60°
B	11	$[1\bar{1}0]$	✓	✓	X	60°
	12	$[1\bar{1}0]$	✓	✓	✓	60°
	13	$[1\bar{1}0]$	✓	✓	✓	60°
	14	$[1\bar{1}0]$	✓	✓	✓	60°
	15	$[1\bar{1}0]$	✓	✓	✓	60°
	16	$[1\bar{1}0]$	✓	X	X	90°
	17	$[1\bar{1}0]$	✓	X	X	90°
	18	$[1\bar{1}0]$	✓	X	X	90°
	19	$[110]$	X	✓	X	90°
	20	$[110]$	✓	✓	✓	60°
	21	$[110]$	✓	✓	X	60°

REFERENCES

- M. Friesen, P. Rugheimer, D. E. Savage, M. G. Lagally, D. W. van der Weide, R. Joynt, and M. A. Eriksson, “Practical design and simulation of silicon-based quantum-dot qubits,” *Phys. Rev. B* **67**, 4 (2003).
- L. R. Schreiber and H. Bluhm, “Quantum computation: Silicon comes back,” *Nat. Nanotechnol.* **9**, 966–968 (2014).
- W. M. Witzel, M. S. Carroll, A. Morello, Ł. Cywiński, and S. Das Sarma, “Electron spin decoherence in isotope-enriched silicon,” *Phys. Rev. Lett.* **105**, 187602 (2010).
- M. Veldhorst, J. C. Hwang, C. H. Yang, A. W. Leenstra, B. De Ronde, J. P. Dehollain, J. T. Muhonen, F. E. Hudson, K. M. Itoh, A. Morello, and A. S. Dzurak, “An addressable quantum dot qubit with fault-tolerant control-fidelity,” *Nat. Nanotechnol.* **9**, 981–985 (2014).
- E. Kawakami, P. Scarlino, D. R. Ward, F. R. Braakman, D. E. Savage, M. G. Lagally, M. Friesen, S. N. Coppersmith, M. A. Eriksson, and L. M. Vandersypen, “Electrical control of a long-lived spin qubit in a Si/SiGe quantum dot,” *Nat. Nanotechnol.* **9**, 666–670 (2014).
- M. Friesen, M. A. Eriksson, and S. N. Coppersmith, “Magnetic field dependence of valley splitting in realistic Si/SiGe quantum wells,” *Appl. Phys. Lett.* **89**, 1–4 (2006).
- M. Friesen and S. N. Coppersmith, “Theory of valley-orbit coupling in a Si/SiGe quantum dot,” *Phys. Rev. B* **81**, 1–17 (2010).
- J. W. Matthews and A. E. Blakeslee, “Defects in epitaxial multilayers: I. Misfit dislocations,” *J. Cryst. Growth* **27**, 118–125 (1974).
- K. Ismail, F. K. LeGoues, K. L. Saenger, M. Arafa, J. O. Chu, P. M. Mooney, and B. S. Meyerson, “Identification of a mobility-limiting scattering mechanism in modulation-doped Si/SiGe heterostructures,” *Phys. Rev. Lett.* **73**, 3447–3450 (1994).
- R. People and J. C. Bean, “Calculation of critical layer thickness versus lattice mismatch for $\text{Ge}_x\text{Si}_{1-x}$ /Si strained-layer heterostructures,” *Appl. Phys. Lett.* **47**, 322–324 (1985).
- D. R. Ward, D. Kim, D. E. Savage, M. G. Lagally, R. H. Foote, M. Friesen, S. N. Coppersmith, and M. A. Eriksson, “State-conditional coherent charge qubit oscillations in a Si/SiGe quadruple quantum dot,” *npj Quantum Inf.* **2**, 1–6 (2016).
- L. Becker, P. Storck, T. Schulz, M. H. Zoellner, L. Gaspere, F. Rovaris, A. Marzegalli, F. Montalenti, M. De Seta, G. Capellini, G. Schwalb, T. Schroeder, and M. Albrecht, “Controlling the relaxation mechanism of low strain $\text{Si}_{1-x}\text{Ge}_x$ /Si(001) layers and reducing the threading dislocation density by providing a preexisting dislocation source,” *J. Appl. Phys.* **128**, 215305 (2020).
- D. Hull and D. J. Bacon, “Elastic properties of dislocations,” in *Introduction to Dislocations*, 5th ed., edited by D. Hull and D. J. Bacon (Butterworth-Heinemann, Oxford, 2011), Chap. 4, pp. 63–83.
- Y. B. Bolkhovityanov, A. S. Deryabin, A. K. Gutakovskii, and L. V. Sokolov, “Mechanisms of edge-dislocation formation in strained films of zinc blende and diamond cubic semiconductors epitaxially grown on (001)-oriented substrates,” *J. Appl. Phys.* **109**, 123519 (2011).
- P. M. Marée, J. C. Barbour, J. F. Van Der Veen, K. L. Kavanagh, C. W. Bulle-Lieuwma, and M. P. Vieggers, “Generation of misfit dislocations in semiconductors,” *J. Appl. Phys.* **62**, 4413–4420 (1987).
- E. A. Stach, R. Hull, R. M. Tromp, F. M. Rossi, M. C. Reuter, and J. C. Bean, “In-situ transmission electron microscopy studies of the interaction between dislocations in strained SiGe/Si (001) heterostructures,” *Philos. Mag. A* **80**, 1559–2200 (2000).
- L. B. Freund, “A criterion for arrest of a threading dislocation in a strained epitaxial layer due to an interface misfit dislocation in its path,” *J. Appl. Phys.* **68**, 2073–2080 (1990).
- V. A. Shah, A. Dobbie, M. Myronov, and D. R. Leadley, “Reverse graded SiGe/Ge/Si buffers for high-composition virtual substrates,” *J. Appl. Phys.* **107**, 064304 (2010).
- O. Skibitzki, M. H. Zoellner, F. Rovaris, M. A. Schubert, Y. Yamamoto, L. Persichetti, L. Di Gaspere, M. De Seta, R. Gatti, F. Montalenti, and

G. Capellini, "Reduction of threading dislocation density beyond the saturation limit by optimized reverse grading," *Phys. Rev. Mater.* **4**, 103403 (2020).

²⁰S. Goswami, K. A. Slinker, M. Friesen, L. M. McGuire, J. L. Truitt, C. Tahan, L. J. Klein, J. O. Chu, P. M. Mooney, D. W. Van Der Weide, R. Joynt, S. N. Coppersmith, and M. A. Eriksson, "Controllable valley splitting in silicon quantum devices," *Nat. Phys.* **3**, 41–45 (2007).

²¹P. G. Evans, D. E. Savage, J. R. Prance, C. B. Simmons, M. G. Lagally, S. N. Coppersmith, M. A. Eriksson, and T. U. Schüllli, "Nanoscale distortions of Si quantum wells in Si/SiGe quantum-electronic heterostructures," *Adv. Mater.* **24**, 5217–5221 (2012).

²²G. Bhagavannarayana, P. Zaumseil, and H. Si, "Diffuse x-ray scattering of misfit dislocations at $\text{Si}_{1-x}\text{Ge}_x/\text{Si}$ interfaces by triple crystal diffractometry," *J. Appl. Phys.* **82**, 1172–1177 (1997).